

THz-assisted microscopy of silica matrix for biological materials encapsulation: a theoretical and experimental study

Matteo De Tullio,[†] and Giovanni Novi Inverardi,[‡] Jonathan Houard,[†] Marc Ropitiaux,[¶] Ivan Blum,[†] Francesco Carnovale,[‡] Gianluca Lattanzi,[§] Simone Taioli,^{||} Gustav Eriksson,[⊥] Mats Hulander,[⊥] Martin Andersson,[⊥] Angela Vella,^{*,†} and Tommaso Morresi^{*,||}

[†]*Univ Rouen Normandie, INSA Rouen Normandie, CNRS, Normandie Univ, GPM UMR 6634, F-76000 Rouen, France*

[‡]*Department of Physics, University of Trento and European Centre for Theoretical Studies in Nuclear Physics and Related Areas (ECT*-FBK) and Trento Institute for Fundamental Physics and Applications (TIFPA-INFN), Trento, Italy*

[¶]*Univ Rouen Normandie, GLYCOMÉV UR4358, SFR Normandie Végétal FED 4277, Innovation Chimie Carnot, IRIB, F-76000 Rouen, France.*

[§]*Department of Physics, University of Trento and Trento Institute for Fundamental Physics and Applications (TIFPA-INFN), Trento, Italy*

^{||}*European Centre for Theoretical Studies in Nuclear Physics and Related Areas (ECT*-FBK) and Trento Institute for Fundamental Physics and Applications (TIFPA-INFN), Trento, Italy*

[⊥]*Department of Chemistry and Chemical Engineering, Chalmers University of Technology Gothenburg 41296, Sweden*

E-mail: angela.vella@univ-rouen.fr; morresi@ectstar.eu

Abstract

In this study, we use THz-assisted atom probe tomography (APT) to analyse silica matrices used to encapsulate biomolecules. This technique provides the chemical composition and 3D structure without significantly heating the biosample, which is crucial for studying soft organic molecules such as proteins. Our results show that THz pulses and a positive static field trigger controlled evaporation of silica matrices, enabling 4D imaging with chemical sensitivity comparable to UV laser-assisted APT. To support the interpretation of these experimental results, we devise a computational model based on time-dependent density functional theory to describe the interaction between silica matrices and THz radiation. This model captures the nonlinear dynamics driven by THz-pulses and the interplay between the THz source and the static electric field in real time. This interdisciplinary approach expands the capabilities of APT and holds promise for other THz-based analyses offering new insights into material dynamics in complex biological environments.

Significant progress has been made in the development of powerful tools for visualising protein structures with sub-nano resolution, such as X-ray crystallography¹ and cryogenic electron microscopy.² To gain new insights in the fields of biology and medicine, these 3D spatial characterisation techniques need to be further developed into 4D approaches that would provide information on the local chemical composition as a fourth dimension.

APT is one such 4D imaging technique based on the controlled field evaporation of atoms from a nanometric needle-shaped sample, achieving sub-nanometre spatial resolution and high chemical sensitivity for the entire periodic table and its isotopes.^{3,4} It has already been used to determine protein and biomaterial structures making it a promising technique for biological research.⁵⁻¹⁰ However, a significant drawback of UV laser-assisted APT is the heating of specimens due to the use of a laser beam in the ultraviolet spectral region, which can affect the integrity of soft organic molecules, such as proteins.^{11,12} To address this issue, terahertz (THz) lasers^{13,14} have been proposed as promising candidates for APT-based microscopy, offering high spatial resolution and chemical sensitivity without damaging the structure of

biological samples. In addition, a breakthrough was achieved in sample preparation for encapsulating biological samples at room temperature. In this approach, a physiological solution containing the protein sample and matrix precursor molecules, typically orthosilicates, is dried to obtain a glassy phase⁷ that provides a solid support for measurements with APT without distorting the native protein structure.^{15,16} However, the use of THz-assisted APT has not yet been explored for materials with larger band gaps, and a comprehensive understanding of the interaction of THz pulses with the silica matrix is still lacking.

Therefore, a thorough experimental and theoretical investigation of field emission dynamics under THz pulse illumination is expected to open up significant opportunities for the development of APT and other THz-based analyses, such as time-dependent spectroscopy and THz-driven scanning tunnelling microscopy.^{17,18}

Computational approaches such as molecular dynamics (MD) and ab initio methods are valuable for understanding the principles of APT applied to soft matter. For instance, classical MD simulations have been used to study the early stages of protein embedding processes.¹⁹ However, to investigate THz-based ion field emission through computational modeling, it is essential to explicitly consider the electronic degrees of freedom. In this context, Time-Dependent Density Functional Theory (TDDFT)²⁰ can be combined with MD. Unfortunately, the high computational cost of TDDFT to describe evaporation processes limits the size of the simulated system for a given level of accuracy. Currently, there are few in silico studies applying TDDFT to THz-induced ion field emission, with only a few focusing on the use of UV femtosecond laser pulses²¹ or static methods.²²⁻²⁴

In this work, we present a computational model based on TDDFT to study the silica matrix under an electrostatic field and THz laser irradiation using $\text{Si}(\text{OH})_4$ as a model. $\text{Si}(\text{OH})_4$ is the precursor molecule of the amorphous solid matrix synthesized in this work using the sol-gel method for encapsulating biomolecules.¹⁶ We emphasize the importance of a time-dependent approach to capture the nonlinear effects related to the interaction of the sample with the THz source and static electric field, leading to a dynamical change of

the interaction forces within the sample. This approach allows us to identify the critical THz laser fields and mechanisms for the ion evaporation process of the hydroxyl groups of $\text{Si}(\text{OH})_4$.

We have also carried out experiments to investigate amorphous silica structures using a nanometric needle-shaped specimen. We successfully achieved controlled evaporation of the silica matrix with THz pulses and a positive static field. Our APT setup is equipped with a detection surface for spatially resolved mass spectrometry analysis, providing information about the impact position and time of flight of the ions.²⁵ By controlling the evaporation layer by layer, we reconstructed the 3D atomic positions of the sample and determined the chemical nature by calculating the mass-to-charge ratio.⁴ Our approach allowed us to generate 4D images of the silica sample with a signal-to-noise ratio (S/N) and mass resolution comparable to those of UV laser-assisted APT. The compositional analysis showed a slight decrease in oxygen loss with increasing electric field, which can be partially explained by the charge analysis from numerical calculations. Our study shows that THz-based ion field emission is possible in insulating materials and that the charge state of evaporated atoms at the THz and static field thresholds obtained in our first-principles simulations agrees well with the measured values of the mass spectra.

Silica matrices are amorphous materials with various bonding schemes and substitutional defects. The studied molecule is a realistic model for the typical Si-O bond in silica, and its size allows affordable first-principles calculations. Our numerical simulations evolved the nuclei (ions) using Ehrenfest dynamics,²⁶ and the electronic wave function was propagated using the TDDFT formalism (see Supplementary Information for more details). In this framework, atomic ions and electrons are exposed to tunable external fields, which can be either static (E_{dc}), time-dependent (E_{laser}) or both. The total external field (static + time-dependent) is expressed by:²¹

$$v_{ext}(\mathbf{x}, t) = \mathbf{x} \cdot \hat{\mathbf{e}} \left[E_{\text{dc}} + E_{\text{laser}} \exp\left(-\frac{(t-t_0)^2}{\sigma^2}\right) \cos(\omega t) \right] \quad (1)$$

where $\hat{\mathbf{e}}$ is the polarisation vector, $\frac{\omega}{2\pi} = 5$ THz, $t_0=50$ fs, and $\sigma=20$ fs.

The laser field and molecule interaction is described using the dipole approximation. In our simulations, the box edge is $a = 2$ nm, and the laser wavelength is $\lambda \approx 6 \times 10^4$ nm, satisfying the dipole condition $\lambda \gg a$. All calculations use the OCTOPUS code,^{27,28} with an additional internal function for handling static external fields interacting with ions.

The DFT equilibrium structure of the $\text{Si}(\text{OH})_4$ molecule is used as the starting configuration for the system's temporal evolution. The molecule has a tetrahedral shape with the silicon atom coordinated with four hydroxyl groups.²⁹ The molecule's geometry is shown in Figure 1a. The pair distribution function in the lower part of the figure indicates that at equilibrium, the bond lengths for all O-H and O-Si pairs are equal.

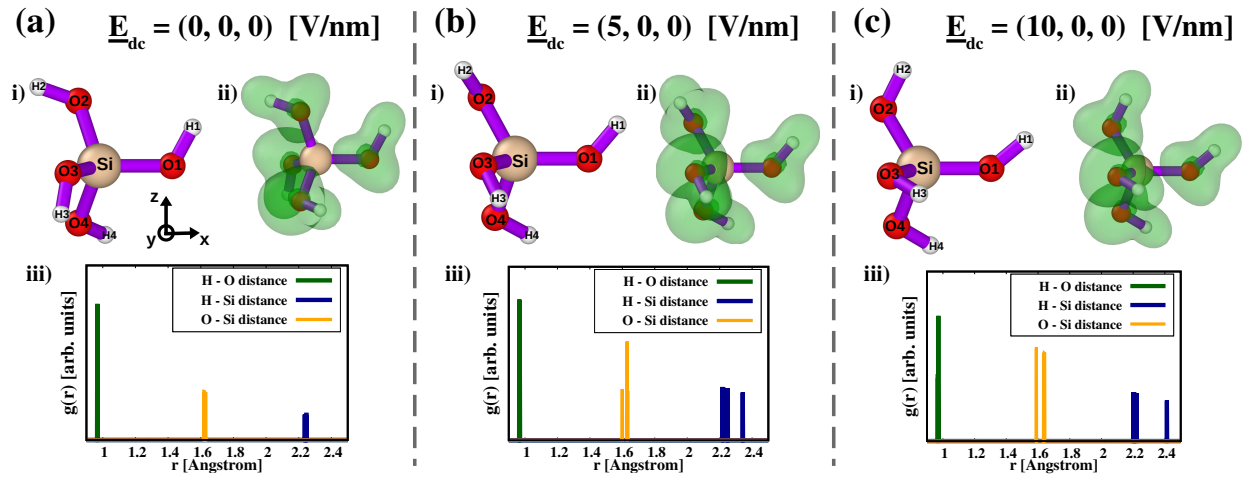


Figure 1: $\text{Si}(\text{OH})_4$ molecule as a function of the static external field: (a) $\mathbf{E}=(0,0,0)$ [V/nm]; (b) $\mathbf{E}=(5,0,0)$ [V/nm]; (c) $\mathbf{E}=(10,0,0)$ [V/nm]. The insets (i) at the top left of panels (a), (b) and (c) are the geometries, while in the insets at the top right (ii) the electron localisation function (ELF) at the isosurface level 0.66 has been added to the structure; the insets at the bottom (iii) show the corresponding pair distribution functions. The geometries were optimised by fixing the Si atom, the y- and z-coordinates of the oxygen atom O1 and the y-coordinate of the corresponding hydrogen atom H1.

When an external static electric field (\mathbf{E}_{dc}) is applied, the molecule polarizes in the direction of the field, as shown in Figures 1b and 1c for fields of $\mathbf{E}_{\text{dc}} = (5,0,0)$ and $\mathbf{E}_{\text{dc}} = (10,0,0)$ [V/nm]. The more intense the static field, the more strongly the hydroxyl groups are oriented in the direction of the field, causing the $\widehat{\text{Si}-\text{O1}-\text{H1}}$ angle in the $\text{Si}(\text{OH})_4$

molecule to increase compared to the unpolarised case (Figure 1a) and the bond distance between Si and O1 to expand to 2.4 Å.

During the dynamics, the positions of the silicon atom and the O2H2, O3H3, and O4H4 ions are fixed to prevent the molecule from drifting. We are particularly interested in the evaporation of the O1 and H1 atoms in response to static and oscillating fields, resembling the evaporation of individual atoms from a solid surface.²¹ For the time-dependent simulations, we focused on two static fields: $E_{dc,x} = 0$ and $E_{dc,x} = 10$ [V/nm] (see Figures 2a,b and c,d) using therefore as initial configurations the geometries in Figures 1a,c respectively. We note that these configurations are only a small subset of the many possible alignments between the external fields and the molecule. We specifically chose the configuration where the O1-Si bond is aligned along the x -axis to uniquely evaluate the contributions of the Coulomb force, static electric field, and time-dependent laser for each value of the external fields. These results should be considered as an upper bound for the real physical system, since different angles between fields and bonds as well as other influencing factors such as defects may exist in reality. We find a clear difference in the behaviour of the system, which of course depends on the intensity of the external fields. Results of the time-dependent simulations are shown in Figure 2. In particular, the distance as function of time between the hydrogen atom H1 and the Si atom is shown in Figures 2a,c and the distance between the oxygen atom O1 and the Si atom in Figures 2b,d. Different symbols represent different laser field intensities.

A laser field with a peak amplitude of 27.5 [V/nm] can evaporate hydrogen in the presence of a static external field of $E_{dc,x} = 10$ [V/nm] (see blue dots in Figure 2c), but not without the static field (Figure 2a). Predicting this behaviour at the static level by calculating the PES is a challenge due to the non-linear interplay between the fields leading to different ionisations of the system. For oxygen, a larger amplitude of 54.5 [V/nm] is required to break the Si-O1 bond, as shown by the red diamonds in Figures 2b,d. The distance between hydrogen and silicon increases rapidly, making it easier to determine the evaporation point,

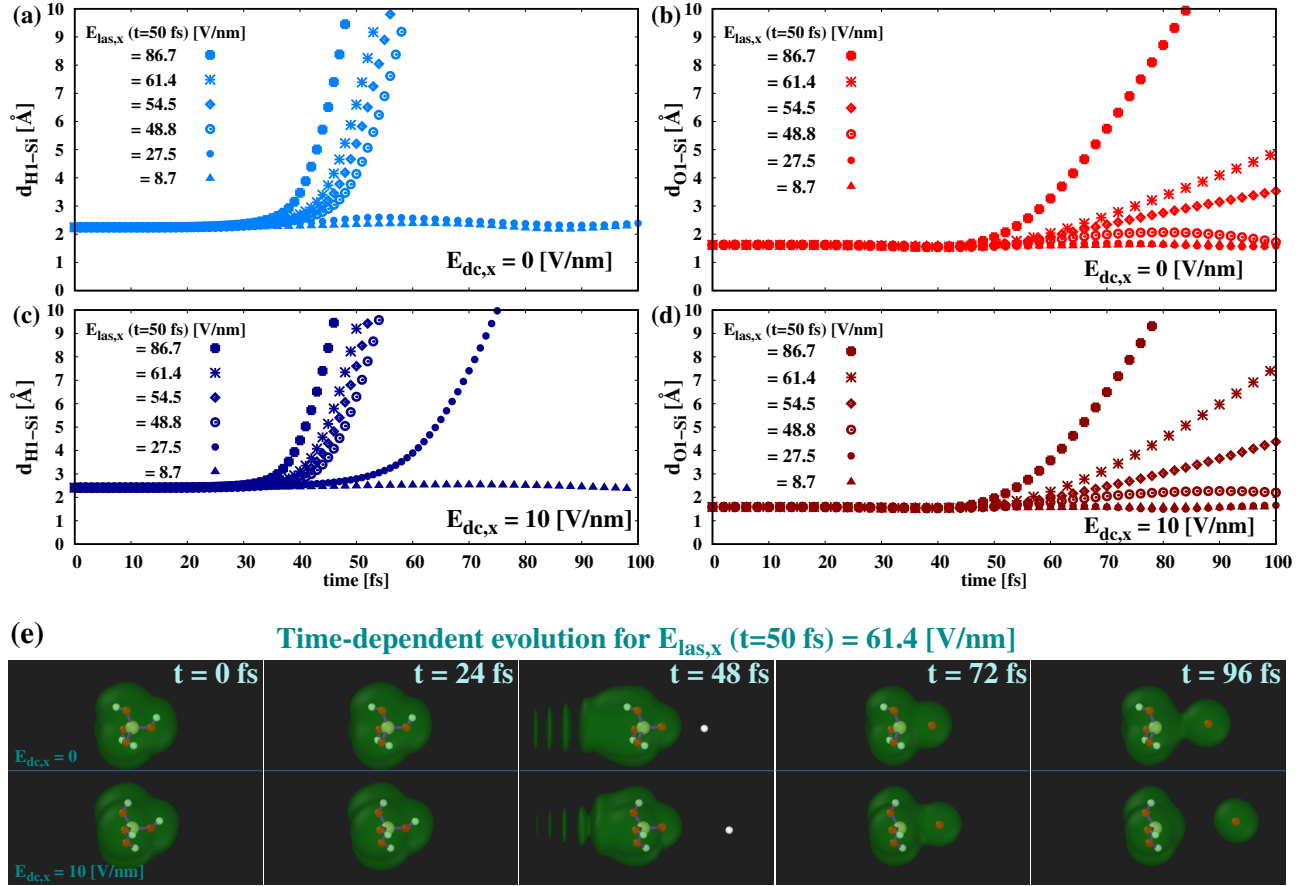


Figure 2: (a,c): Distances between the hydrogen atom H1 and silicon as a function of time. (b,d): Distances between the oxygen atom O1 and silicon as a function of time. The labels follow the convention of Figure 1. (e) Plot of the electronic density's isosurface equal to 10^{-4} and ions for five different snapshots of the time evolution in the case of $E_{\text{laser},x}(t = 50 \text{ fs}) = 61.4$ [V/nm]; the upper plots report the evolution without static electric field while the lower ones with $E_{\text{dc},x} = 10$ [V/nm].

while the slower increase in the distance of oxygen from silicon makes it more difficult to determine the evaporation point within the time frame of our simulations.

Nevertheless, our ab initio calculations provide information about the forces and velocities acting on the atoms allowing us to determine the kinetic energy of the oxygen atom. The analysis of this information, together with the charge density, reveals the primary role of ionisation in the evaporation of oxygen. Intense laser fields lead to increased ionisation of the fixed part of the molecule. As the evaporating H1 and O1 atoms are always positively charged, this results in a stronger Coulomb repulsion between the evaporating atoms and the fixed part of the molecule, pushing the atoms far away, even in the absence of static external fields. Figure 2e shows the electronic density at the isosurface level 10^{-4} as well as the ions for a peak laser amplitude of 61.4 [V/nm] in the absence of a static field (upper plot) and in the presence of $E_{dc,x} = 10$ [V/nm] (lower plot). The snapshots illustrate the density at different

Table 1: Summary of the results from the Ehrenfest dynamics simulations. d_{H1-Si} and d_{O1-Si} are the distances between the hydrogen atom H1 and the Si atom and between the oxygen atom O1 and the Si atom; N_{mol}^* is the final total charge of the fixed molecule, while N_{O1}^* and N_{H1}^* are the charges of the evaporating oxygen and hydrogen atoms. The latter two values are only given if the distances between these atoms and the Si are greater than 3 Å. The number of electrons emitted is calculated as $N_{mol}^* + N_{O1}^* + N_{H1}^*$.

$E_{dc,x}$ [$\frac{V}{nm}$]	$E_{las,x}(t = 50 fs)$ [$\frac{V}{nm}$]	N_{mol}^*	N_{H1}^*	N_{O1}^*	d_{H1-Si} [Å]	d_{O1-Si} [Å]
0	8.7	0.0	-	-	2.30	1.61
10	8.7	0.1	-	-	2.36	1.59
0	27.5	0.8	-	-	2.39	1.58
10	27.5	0.6	1.0	-	> 10	1.58
0	41.1	1.2	1.0	-	> 10	1.60
10	41.1	2.0	1.0	-	> 10	1.49
0	48.8	1.6	1.0	-	> 10	1.71
10	48.8	2.6	1.0	-	> 10	2.20
0	54.5	2.4	1.0	0.5	> 10	3.52
10	54.5	2.5	1.0	0.9	> 10	4.37
0	61.4	2.7	1.0	0.7	> 10	4.88
10	61.4	2.8	1.0	1.0	> 10	6.27
0	86.7	3.9	1.0	1.9	> 10	> 10
10	86.7	4.0	1.0	2.1	> 10	> 10

time steps of the simulation. As expected, the static field clearly accelerates the escaping

hydrogen and oxygen atoms. Additionally, we observe a significant difference in the charge densities of the same oxygen atom with and without a static field. The results for the charge state and distance reached by the atoms at the end of the simulation are summarised in Table 1. We observed that the hydrogen atom always evaporates fully ionised with a charge of +1, while the charge of the evaporated oxygen atom increases with the laser amplitude. This theoretical prediction is supported by our analysis of the mass spectra. We also stress that, despite the analysis of an isolated molecule without defects, the critical amplitudes of THz-fields for evaporating H1 and O1 are close to the experimental values¹³ as shown below.

On the experimental side, the silica samples were prepared using a lift-out procedure with a focused ion beam scanning electron microscope (FIB-SEM)^{30,31} to cut the matrix into a thin needle shape with a radius of less than 100 nm (more details in the Supplementary Information).

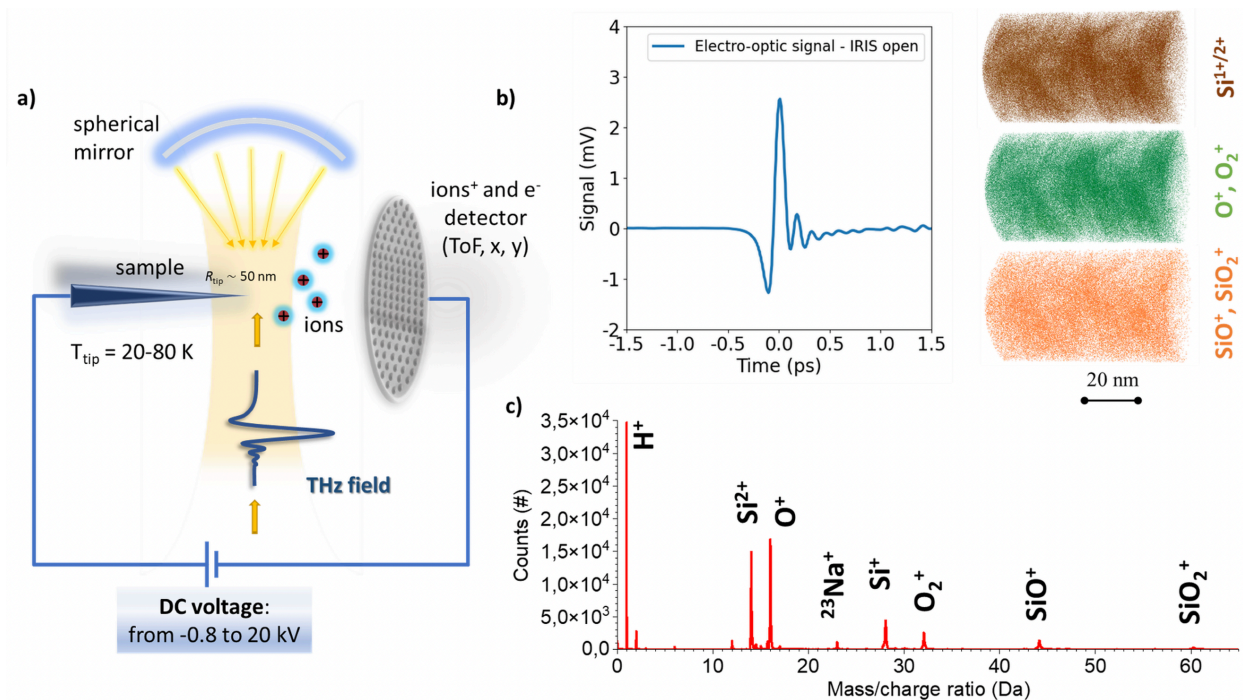


Figure 3: **(a)** Schematic representation of a THz-assisted APT analysis chamber. **(b)** Left panel: Measured electro-optical signal. Right panel: 3D atomic distribution of Si (brown dots), oxygen atoms (green dots) and silicon dioxide (orange dots), reconstructed with a starting radius of 25 nm and a cone angle of 1.5°. **(c)** Mass spectrum of a silica sample (data recorded on 1.1×10^6 atoms).

The spatially resolved mass spectrum is measured with a THz-assisted APT system, as shown in Figure 3a.³² The nanometric needle-shaped specimen is polarised with a DC voltage of -0.8 kV to 20 kV, resulting in an apex electric field of over 10 V/nm. The atoms in the layers of the sample are evaporated due to the strong electrostatic field and the irradiation with single-cycle THz pulses, which trigger the evaporation process.¹³ Single-cycle THz pulses are generated by a two-color laser field-induced plasma in N₂.^{33,34} The THz pulses have a repetition rate of 1 kHz, matching that of the two-color laser system, which consists of the fundamental harmonic (FH) and the second harmonic (SH) of the 800 nm wavelength laser. The amplitude of the THz pulses is proportional to the input power of the FH, which can be adjusted at the entry of the plasma. The THz fields are predominantly generated by asymmetric electron currents triggered by photoionisation in N₂ gas. The generated THz field is characterized via electro-optical (EO) scanning in a non-linear crystal before it is focused on the APT sample. An example of the EO signal is presented in Figure 3b on the left, where a signal of 3 mV corresponds to an electric field of 20 MV/m. The THz pulse is then amplified by a factor of several thousand at the apex of the sample, as shown in previous works on metallic and non-metallic samples.^{14,35} Therefore, the maximum THz field amplitude ranges between 5-30 V/nm (further details in the Supplementary Information).

After evaporation, ions are directed onto a detection surface using an electrostatic field. The detector provides information about the impact position and time of flight of the ions,²⁵ enabling the reconstruction of the 3D structure of the sample. Each ejected ion is assigned an initial position through back-projection, as shown in Figure 3b and its chemical nature is determined by calculating the mass-to-charge state ratio, as shown in the mass spectrum of Figure 3c.⁴ The 3D distribution of silicon, silica (SiO and SiO₂), and oxygen atoms is reconstructed by in-house software, with observed inhomogeneity attributed to the porosity of the amorphous silica sample.

Figure 4 displays the results from the homogeneous part of a second silica sample. The THz amplitude was maintained at its maximum during the analysis, and the DC voltage

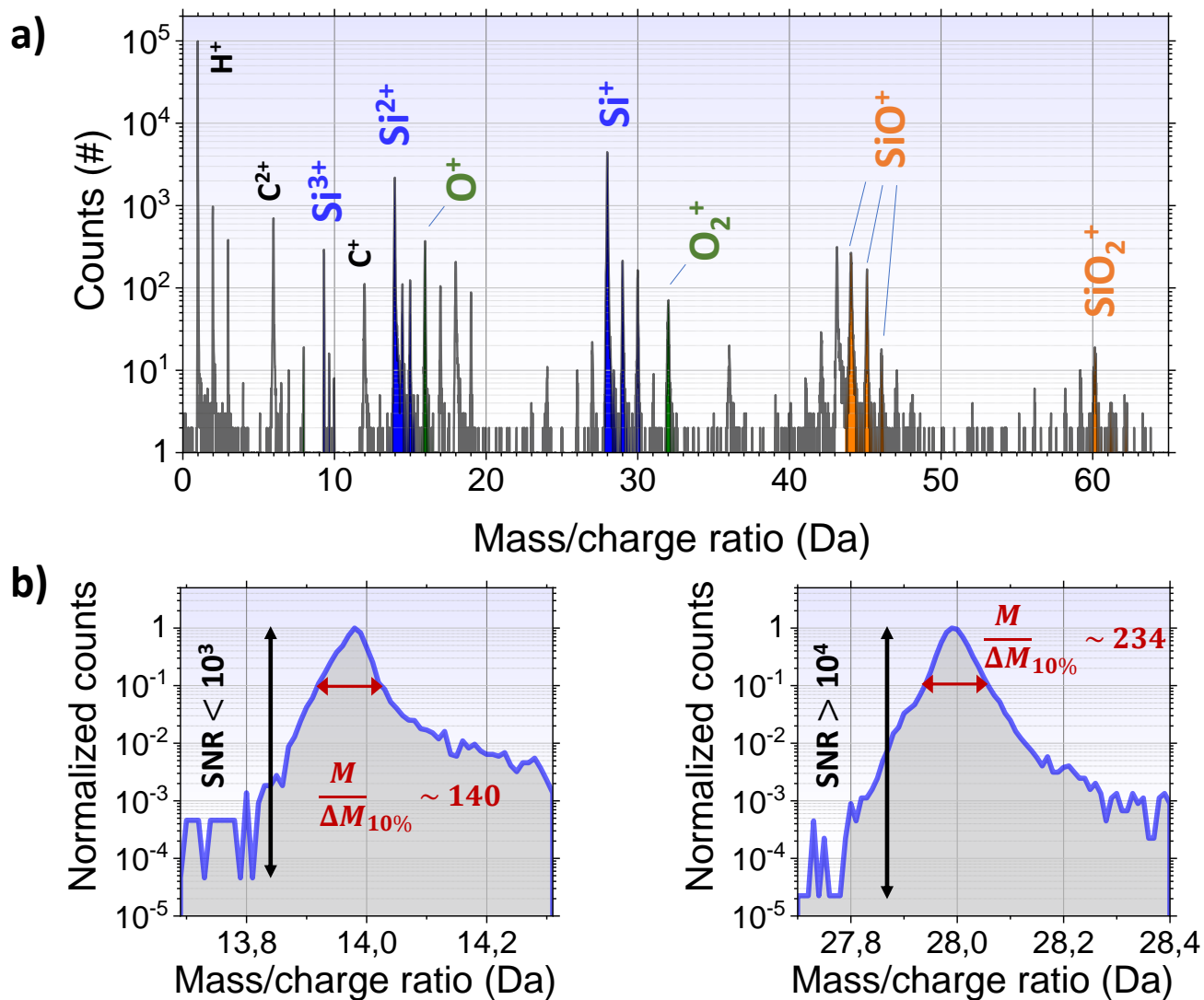


Figure 4: (a) Mass spectrum of the silica sample in the range 0-65 Da. (b) Focus on the normalized Si^{2+} peak at 14 Da and Si^+ peak at 28 Da. Data set of 250k atoms.

was automatically adjusted to ensure a constant detection rate during the field evaporation process, as shown in Figure 4b.

The mass spectrum (Figure 4a) exhibits characteristic peaks of silicon in the 2+ charge state at 14, 14.5, and 15 Da and in the 1+ state at 28, 29, and 30 Da. Additionally, peaks of molecular ions of silica, SiO and SiO₂, are observed at 44 and 60 Da for the 1+ charge state and less prominently at 22 and 30 Da for the 2+ state. The peak at 30 Da overlaps with the ³⁰Si⁺ isotope, which affects the natural isotopic distribution for the peaks at 28, 29 and 30 Da. The spectrum also indicates the presence of platinum in the 2+ state and carbon in both the 1+ and 2+ states, likely from the C₉H₁₆Pt gas used in the sample preparation by FIB-SEM milling. A peak at 23 Da suggests the presence of sodium, likely a residue from the sol-gel preparation.

We see a peak at 17 Da for the OH⁺ ion, but there are 100 times fewer of these ions than O⁺, indicating a low probability of evaporation. This is consistent with our ab-initio simulation results, which also did not show evaporation of these ions.

The Si²⁺ and Si⁺ peaks (Fig. 4 (b)) have a signal to noise ratio (SNR) larger than 10³ and a mass resolution at 10% of the peak maximum of 140 and 234, respectively. These values are comparable to those obtained with UV laser-assisted APT on oxides.^{36,37} The asymmetry of the Si²⁺ and Si⁺ peaks, with a long tail on the right side, suggests that thermal effects contribute to the evaporation process

In the second set of analyses we increased the DC voltage and observed a corresponding decrease in THz amplitude (Figure 5c). This was done to maintain a constant detection rate and to study how the sample evaporation changes. Figure 5a shows the mass-to-charge state ratio and detection rate against the sequence of evaporated atoms, capturing the temporal progression of the analysis. Slight shifts in the mass spectrum lines were observed, not directly corresponding to changes in flux but associated with the change in THz amplitude. The decrease in THz pulse corresponds to a decrease in the average energy of the ions,¹⁴ leading to a shift towards high Da values in the mass spectrum. The detection rate tends to

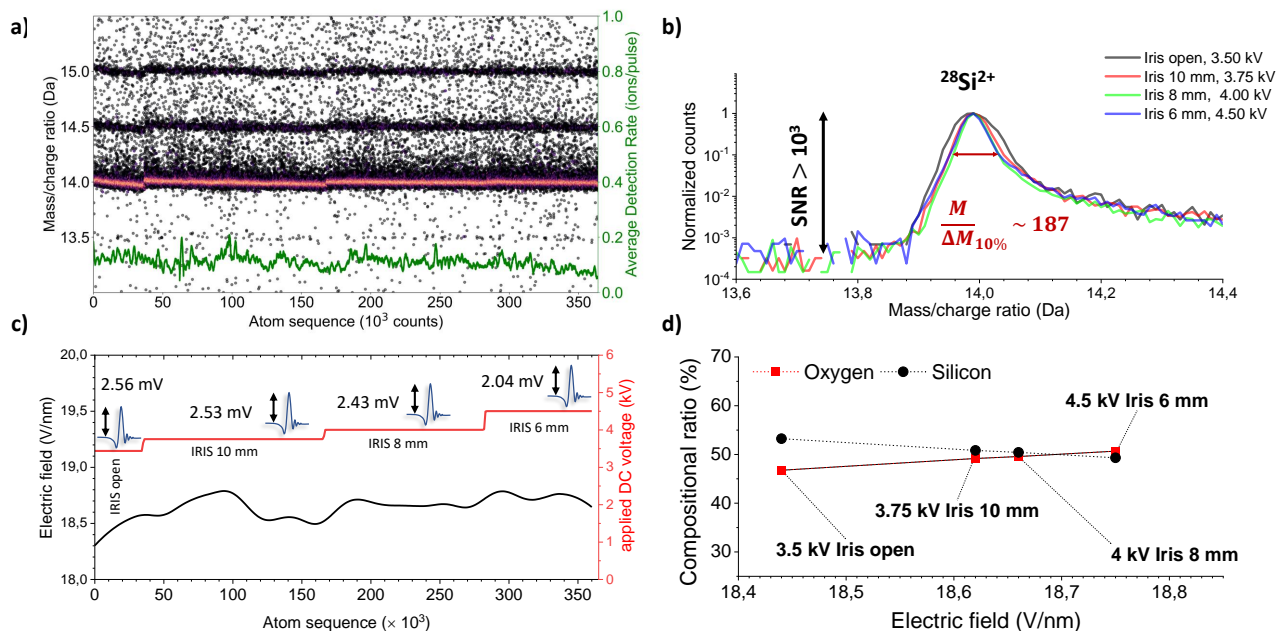


Figure 5: **(a)** Joint plot of the mass-to-charge ratio (as density plot) and the detection rate (green line) as a function of the temporal progression of the analysis on a data set of 360k ions in the range 13-15.5 Da to emphasize the Si^{2+} species. **(b)** Focus on the normalized Si^{2+} peak at 14 Da. A signal-to-noise ratio of more than 10^3 was measured. A THz amplitude of 2.43 mV in combination with a DC bias voltage of 4 kV provided the optimal mass resolving power at both 14 Da. **(c)** Red line: DC voltage temporal trend coupled with the THz signal amplitudes used in each case; black line: temporal progression of the electric field of the tip surface. **(d)** Total compositional ratio of silicon and oxygen as a function of the electric field on the tip surface.

decrease when the THz field amplitude decreases by about 20%, despite a 20% increase in DC voltage. We used the Si^+ to Si^{2+} count ratio to calculate the surface field at the top of our sample, as per Kingham’s post-ionisation theory.³⁸ However, the field calculation shows a slight but costly increase in the field. This indicates that the evaporation process has a non-linear behavior depending on the THz field, as confirmed by our TDDFT simulations. We intentionally avoided increasing the DC voltage further to prevent tip fracture from mechanical stress.³⁹

The Si^{2+} peaks in Figure 5b have a mass resolution at 10% of the peak maximum of 187, which is consistent across all analysis conditions.

Figure 5d shows the analysis of the composition as a function of the electric field on the tip surface. The resulting composition deviates from the expected nominal ratio in silica of 66.6% oxygen and 33.3% silicon, instead showing a tendency towards an equal distribution of 50% oxygen and 50% silicon, suggesting an oxygen deficit during the evaporation process. The peak at 16 Da can be attributed to either O_2^{2+} or O_1^+ . If the peak at 16 Da were attributed to O_2^{2+} , the total oxygen content would increase to 66%, which is the nominal composition. However, APT analysis of ^{18}O -enriched $\alpha\text{-Fe}_2\text{O}_3$ ruled out the evaporation of the O_2^{2+} species and confirmed the presence of O_1^+ .⁴⁰ DFT simulations predict the evaporation of the O_1^+ species and the migration of O_1^- in the cluster, potentially leading to the formation of O_2 and subsequent evaporation as O_2^{2+} .⁴¹

Previous research has shown that a fraction of oxygen is lost in UV laser APT analysis of oxides, suggesting that it evaporates as a neutral entity rather than a positively charged ion.⁴² Furthermore, our results indicate that changes in electric field had no significant effect on the composition of the molecular species (see Supplementary Information).

In summary, in our study we used THz-assisted APT to analyze the chemical and structural properties of silica matrices for encapsulating biomolecules. This approach does not cause significant heating of the sample and enables high-resolution 4D imaging with high chemical sensitivity, revealing the emission of single ionic species over molecular ions. Our

results agree with TDDFT calculations, showing a significant change in charge density with applied static fields. In particular, first-principles simulations indicate that oxygen can be evaporated by THz field of 54 V/nm in 50 fs, at odds with previous predictions of 0.5-3 ps.⁴³⁻⁴⁵ New simulations are planned to investigate the evaporation of O₂ molecular ions and the formation of negatively charged oxygen atoms. This interdisciplinary approach demonstrates the potential of THz-assisted APT for advanced microscopy of nanoscale surface features, including in biological environments.

Acknowledgement

This action has received funding from the European Union under grant agreement n. 101046651. MA acknowledges the support of the Swedish Research Council (VR) and the Knut and Alice Wallenberg Foundation through their Wallenberg Academy Fellows program.

Supplementary Information

Sample Synthesis

The silica samples were prepared according to a protocol developed for silica encapsulation of proteins for APT analysis.⁷ In all experimental steps, the water used was filtered through a Milli-Q (Millipore) system. All chemicals were purchased from Sigma-Aldrich and used without further purification. A sodium silicate solution (25.5 - 28.5 % SiO₂ 7.5 - 8.5 % Na₂O), also known as water glass, was used to form silica through a sol-gel process. Gelling was initiated by adjusting the pH of the sodium silicate solution from alkaline to physiological (pH 7.4). For this purpose, an acidic ion exchange column was prepared by adding 1 g of ion exchange resin (Dowex 50WX8 hydrogen form 50-100 mesh, Sigma-Aldrich) to 0.5 g of glass wool in a 10 mL plastic syringe. The ion exchange resin was activated by washing with 10 mL NaOH (4 M), followed by water and finally 10 mL HCl (1 M). The activity was adjusted by rinsing with small amounts of water until the eluate had a neutral pH. The original sodium silicate solution was then diluted with water in a volume ratio of 1:3 before 1 mL of the solution was passed through the column, collected in a vial and allowed to harden in an open vial at 37 °C for ≥ 48 h to obtain a solid silicate material.

Experimental Setup

Experiments were conducted in a custom-built ultrahigh vacuum chamber with a 10 cm flight path and a base pressure of 5×10^{-11} mbar. The sample was cooled to 50 K using a compression cryostat and polarized with a positive applied DC bias, resulting in an intense field at the tip apex.

Field ion evaporation was initiated by a THz pulse generated by a two-color ultra-short laser pulse. The laser system used was a Spitfire model from Spectra Physics, which produced a 45-fs pulse in the infrared at a wavelength of 800 nm, with a repetition rate of 1 kHz and a maximum energy of 3.5 mJ. The output beam was a TEM00 Gaussian beam with a diameter

of 8 mm. The beam was split into two parts (90/10 in energy); the higher-energy beam was used for terahertz generation and was mechanically chopped at 145 Hz. The lower-energy beam was used as a probe for the temporal characterization of the terahertz pulses in an EO sampling setup based on a GaP crystal outside the APT chamber. The terahertz pulse was generated by a two-color plasma generation process.³³

The NIR laser beam was focused in air by a 40 cm focal lens and passed through a BBO crystal placed before the focal plane to generate the second harmonic at 400 nm. The focused bi-chromatic femtosecond laser pulses emitted THz radiation with very high field strengths. The energy of the second harmonic was fixed at 2.65 mJ, corresponding to an intensity of 3×10^{15} W cm². The amplitude of the emitted THz pulses could be controlled by changing the aperture diameter of the pump beam. The produced THz field was then focused on the sample inside the APT ultra-vacuum chamber.

Surface atoms were ionized by the combined action of the DC field and the THz pulse and left the surface, flying toward a detector sensitive to the impact position of the ion and its time of flight. The time of flight of the ions allowed for the identification of their mass/charge ratio, i.e., (with some limitations) their chemical identity. Furthermore, the impact position on the detector made it possible to reconstruct the original position of each ion on the tip through a back-projection algorithm. The Position Sensitive Detector (PSD) was a delay line detector with improved multihit capabilities. It consisted of a conventional 8 cm Roentdek delay line detector following a pair of microchannel plates (MCPs) in chevron configuration. Signal output from each end of the two wire pairs was digitized by means of fast digitizer boards PXI DC 271 (or Keysight U1051A Acquiris). Ion flight time signals were taken as output from the MCP, and the positioning was calculated using signals provided by the delay line outputs. A deconvolution algorithm was used to improve the multihit capabilities of the PSD.²⁵

Theoretical and computational details

The coupled electron-nuclear dynamics is formulated as follows (a.u. are adopted):²⁰

$$i \frac{\partial \phi_j(\mathbf{r}, t)}{\partial t} = \left[-\frac{\nabla^2}{2} + v_{ext}(\mathbf{r}, t) + v_{H,xc}(\mathbf{r}, t) + \hat{W}_{en}(\{\mathbf{r}\}, \{\mathbf{R}(t)\}) \right] \phi_j(\mathbf{r}, t) \quad (2)$$

$$M_J \frac{\partial^2 \mathbf{R}_J}{\partial t^2} = -\nabla_{\mathbf{R}_J} \left[v_{ext}(\mathbf{R}_J, t) + \hat{W}_{nn}(\{\mathbf{R}(t)\}) + \int d^3r n(\mathbf{r}, t) \hat{W}_{en}(\{\mathbf{r}\}, \{\mathbf{R}(t)\}) \right] \quad (3)$$

where ϕ_j is the electronic wave function of the occupied orbitals, v_{ext} is external scalar potential acting on both electrons at position $\{\mathbf{r}\}$ and nuclei at position $\{\mathbf{R}\}$, $v_{H,xc}$ is the Hartree plus exchange-correlation potential, \hat{W}_{nn} is the Coulomb interaction between the nuclei, M_J is the mass of the J -th nucleus, \hat{W}_{en} is the Coulomb interaction between the electrons and the nuclei, and $n(\mathbf{r}, t) \equiv \sum_j^{occ} |\phi_j(\mathbf{r}, t)|^2$ is the electron density.

The TDDFT simulation box for the $\text{Si}(\text{OH})_4$ molecule is a 20 Å cube, which was chosen to ensure that the TDDFT simulation preserves the energy of the system without a laser field. The real space mesh spacing is 0.16 Å, resulting in a total energy convergence below 5 meV. To prevent the electrons emitted by the laser from being reflected at the edges of the box, we implement absorbing boundary conditions that suppress the electronic density. For this purpose, we use a mask function that is equal to one in the inner region and smoothly decreases to zero in the edge region. For the TDDFT simulations, the time step integrator is equal to $4 \cdot 10^{-4}$ fs and in Eq. 1 we use $t_0=50$ fs (corresponding to the maximum amplitude of the laser signal) and $\sigma=20$ fs.²¹ The ion trajectories and the electron wave functions are propagated for 100 fs, through $2.5 \cdot 10^5$ total steps.

The initial geometries reported in Figure 1 were optimized using the FIRE algorithm⁴⁶ with a force threshold of 0.03 eV/Å. To prevent global translations and rotations of the molecule in the presence of the static external field, the optimizations were carried out by

fixing the central Si atom, the y and z coordinates of the oxygen atom O1, and the y coordinates of the hydrogen atom H1 (see Figure 1). The static electric field values analysed in this work are $\mathbf{E}_{\text{dc}} = (0, 0, 0)$, $\mathbf{E}_{\text{dc}} = (5, 0, 0)$ and $\mathbf{E}_{\text{dc}} = (10, 0, 0)$ [$\frac{\text{V}}{\text{nm}}$]. It is worth noting that the maximum (and minimum) value of the static fields was chosen so that the electrons bound for $\mathbf{E}_{\text{dc}} = 0$ remain bound to the molecule even in the presence of the static external field. The explicit treatment of the electric field is necessary to prevent the global minimum of the potential for the electrons from moving to the edge of the box when the amplitude of the field is large enough. Although this can be avoided by treating electric fields in the framework of the modern polarisation theory,⁴⁷ we retain the explicit treatment of \mathbf{E}_{dc} because it has been shown in previous investigations²¹⁻²⁴ to be useful for describing the evaporation dynamics of atoms from molecules and periodic systems.

The nuclear-electron interaction is modeled using the pseudopotential method within the local density approximation (LDA)⁴⁸ for the static DFT electron exchange-correlation and the adiabatic LDA (ALDA) for the TDDFT simulations. In this framework, the $\text{Si}(\text{OH})_4$ molecule has 32 valence electrons.

References

- (1) Smyth, M.; Martin, J. x Ray crystallography. *Molecular Pathology* **2000**, *53*, 8.
- (2) Bai, X.-C.; McMullan, G.; Scheres, S. H. How cryo-EM is revolutionizing structural biology. *Trends in biochemical sciences* **2015**, *40*, 49–57.
- (3) Gault, B.; Vurpillot, F.; Vella, A.; Gilbert, M.; Menand, A.; Blavette, D.; Deconihout, B. Design of a femtosecond laser assisted tomographic atom probe. *Review of Scientific Instruments* **2006**, *77*, 043705.
- (4) Kelly, T. F.; Miller, M. K. Atom probe tomography. *Review of scientific instruments* **2007**, *78*.

- (5) Grandfield, K.; Micheletti, C.; Deering, J.; Arcuri, G.; Tang, T.; Langelier, B. Atom probe tomography for biomaterials and biomineralization. *Acta Biomaterialia* **2022**, *148*, 44–60.
- (6) Perea, D. E.; Liu, J.; Bartrand, J.; Dicken, Q.; Thevuthasan, S. T.; Browning, N. D.; Evans, J. E. Atom probe tomographic mapping directly reveals the atomic distribution of phosphorus in resin embedded ferritin. *Scientific reports* **2016**, *6*, 22321.
- (7) Sundell, G.; Hulander, M.; Pihl, A.; Andersson, M. Atom probe tomography for 3D structural and chemical analysis of individual proteins. *Small* **2019**, *15*, 1900316.
- (8) Qiu, S.; Zheng, C.; Garg, V.; Chen, Y.; Gervinskas, G.; Li, J.; Dunstone, M. A.; Marceau, R. K.; Fu, J. Three-dimensional chemical mapping of a single protein in the hydrated state with atom probe tomography. *Analytical chemistry* **2020**, *92*, 5168–5177.
- (9) Sundell, G.; Dahlin, C.; Andersson, M.; Thuvander, M. The bone-implant interface of dental implants in humans on the atomic scale. *Acta biomaterialia* **2017**, *48*, 445–450.
- (10) Karlsson, J.; Sundell, G.; Thuvander, M.; Andersson, M. Atomically resolved tissue integration. *Nano letters* **2014**, *14*, 4220–4223.
- (11) Vella, A.; Silaeva, E. P.; Houard, J.; Itina, T. E.; Deconihout, B. Probing the thermal response of a silicon field emitter by ultra-fast Laser Assisted Atom Probe Tomography. *Annalen der Physik* **2013**, *525*, L1–L5.
- (12) Houard, J.; Vella, A.; Vurpillot, F.; Deconihout, B. Three-dimensional thermal response of a metal subwavelength tip under femtosecond laser illumination. *Physical Review B* **2011**, *84*, 033405.
- (13) Vella, A.; Houard, J.; Arnoldi, L.; Tang, M.; Boudant, M.; Ayoub, A.; Normand, A.; Da Costa, G.; Hideur, A. High-resolution terahertz-driven atom probe tomography. *Science Advances* **2021**, *7*, eabd7259.

- (14) Karam, M.; Houard, J.; Damarla, G.; Rousseau, L.; Bhorade, O.; Vella, A. THz driven field emission: energy and time-of-flight spectra of ions. *New Journal of Physics* **2023**, *25*, 113017.
- (15) McCarroll, I. E.; Bagot, P.; Devaraj, A.; Perea, D. E.; Cairney, J. New frontiers in atom probe tomography: a review of research enabled by cryo and/or vacuum transfer systems. *Materials Today Advances* **2020**, *7*, 100090.
- (16) Sundell, G.; Hulander, M.; Pihl, A.; Andersson, M. Atom Probe Tomography for 3D Structural and Chemical Analysis of Individual Proteins. *Small* **2019**, *15*, 1900316.
- (17) Cocker, T. L.; Jelic, V.; Gupta, M.; Molesky, S. J.; Burgess, J. A.; Reyes, G. D. L.; Titova, L. V.; Tsui, Y. Y.; Freeman, M. R.; Hegmann, F. A. An ultrafast terahertz scanning tunnelling microscope. *Nature Photonics* **2013**, *7*, 620–625.
- (18) Wimmer, L.; Herink, G.; Solli, D. R.; Yalunin, S. V.; Echterkamp, K. E.; Ropers, C. Terahertz control of nanotip photoemission. *Nature Physics* **2014**, *10*, 432–436.
- (19) Novi Inverardi, G.; Carnovale, F.; Petrolli, L.; Taioli, S.; Lattanzi, G. Silica In Silico: A Molecular Dynamics Characterization of the Early Stages of Protein Embedding for Atom Probe Tomography. *Biophysica* **2023**, *3*, 276–287.
- (20) Ullrich, C. A. *Time-Dependent Density-Functional Theory: Concepts and Applications*; Oxford University Press, 2012.
- (21) Silaeva, E. P.; Uchida, K.; Suzuki, Y.; Watanabe, K. Energetics and dynamics of laser-assisted field evaporation: Time-dependent density functional theory simulations. *Phys. Rev. B* **2015**, *92*, 155401.
- (22) Feibelman, P. J. Surface-diffusion mechanism versus electric field: Pt/Pt(001). *Phys. Rev. B* **2001**, *64*, 125403.

- (23) Sánchez, C. G.; Lozovoi, A. Y.; Alavi, A. Field-evaporation from first-principles. *Molecular Physics* **2004**, *102*, 1045–1055.
- (24) Tamura, H.; Tsukada, M.; McKenna, K. P.; Shluger, A. L.; Ohkubo, T.; Hono, K. Laser-assisted field evaporation from insulators triggered by photoinduced hole accumulation. *Phys. Rev. B* **2012**, *86*, 195430.
- (25) Costa, G. D.; Wang, H.; Duguay, S.; Bostel, A.; Blavette, D.; Deconihout, B. Advance in multi-hit detection and quantization in atom probe tomography. *Review of Scientific Instruments* **2012**, *83*.
- (26) Marx, D.; Hutter, J. *Ab Initio Molecular Dynamics: Basic Theory and Advanced Methods*; Cambridge University Press, 2009; p 11–84.
- (27) Andrade, X. et al. Real-space grids and the Octopus code as tools for the development of new simulation approaches for electronic systems. *Phys. Chem. Chem. Phys.* **2015**, *17*, 31371–31396.
- (28) Tancogne-Dejean, N. et al. Octopus, a computational framework for exploring light-driven phenomena and quantum dynamics in extended and finite systems. *The Journal of Chemical Physics* **2020**, *152*, 124119.
- (29) Belton, D.; Deschaume, O.; Perry, C. An overview of the fundamentals of the chemistry of silica with relevance to biosilicification and technological advances. *FEBS J* **2012**, *279*, 1710–1720.
- (30) Miller, M.; Russell, K.; Thompson, G. Strategies for fabricating atom probe specimens with a dual beam FIB. *Ultramicroscopy* **2005**, *102*, 287–298.
- (31) Thompson, K.; Lawrence, D.; Larson, D.; Olson, J.; Kelly, T.; Gorman, B. In situ site-specific specimen preparation for atom probe tomography. *Ultramicroscopy* **2007**, *107*, 131–139.

- (32) Blavette, D.; Bostel, A.; Sarrau, J.-M.; Deconihout, B.; Menand, A. An atom probe for three-dimensional tomography. *Nature* **1993**, *363*, 432–435.
- (33) Bartel, T.; Gaal, P.; Reimann, K.; Woerner, M.; Elsaesser, T. Generation of single-cycle THz transients with high electric-field amplitudes. *Optics Letters* **2005**, *30*, 2805–2807.
- (34) Kim, K.-Y.; Glowina, J. H.; Taylor, A. J.; Rodriguez, G. Terahertz emission from ultrafast ionizing air in symmetry-broken laser fields. *Optics express* **2007**, *15*, 4577–4584.
- (35) Houard, J.; Arnoldi, L.; Ayoub, A.; Hideur, A.; Vella, A. Nanotip response to monocycle terahertz pulses. *Applied Physics Letters* **2020**, *117*.
- (36) Marquis, E. A.; Yahya, N. A.; Larson, D. J.; Miller, M. K.; Todd, R. I. Probing the improbable: Imaging C atoms in alumina. *Materials Today* **2010**, *13*, 34–36.
- (37) Vella, A.; Mazumder, B.; Da Costa, G.; Deconihout, B. Field evaporation mechanism of bulk oxides under ultra fast laser illumination. *Journal of Applied Physics* **2011**, *110*.
- (38) Kingham, D. R. The post-ionization of field evaporated ions: A theoretical explanation of multiple charge states. *Surface Science* **1982**, *116*, 273–301.
- (39) Rigutti, L.; Venturi, L.; Houard, J.; Normand, A.; Silaeva, E. P.; Borz, M.; Malykhin, S. A.; Obraztsov, A. N.; Vella, A. Optical Contactless Measurement of Electric Field-Induced Tensile Stress in Diamond Nanoscale Needles. *Nano Letters* **2017**, *17*, 7401–7409, PMID: 29095635.
- (40) Bachhav, M.; Danoix, F.; Hannoyer, B.; Bassat, J. M.; Danoix, R. Investigation of O-18 enriched hematite (α -Fe₂O₃) by laser assisted atom probe tomography. *International Journal of Mass Spectrometry* **2013**, *335*, 57–60.

- (41) Karahka, M.; Kreuzer, H. Field evaporation of oxides: A theoretical study. *Ultramicroscopy* **2013**, *132*, 54–59, IFES 2012.
- (42) Mancini, L.; Amirifar, N.; Shinde, D.; Blum, I.; Gilbert, M.; Vella, A.; Vurpillot, F.; Lefebvre, W.; Lardé, R.; Talbot, E.; others Composition of wide bandgap semiconductor materials and nanostructures measured by atom probe tomography and its dependence on the surface electric field. *The Journal of Physical Chemistry C* **2014**, *118*, 24136–24151.
- (43) Müller, E. W. Field Desorption. *Phys. Rev.* **1956**, *102*, 618–624.
- (44) Gomer, R. Field Desorption. *The Journal of Chemical Physics* **2004**, *31*, 341–345.
- (45) Kellogg, G. Measurement of activation energies for field evaporation of tungsten ions as a function of electric field. *Physical Review B* **1984**, *29*, 4304.
- (46) Bitzek, E.; Koskinen, P.; Gähler, F.; Moseler, M.; Gumbsch, P. Structural Relaxation Made Simple. *Phys. Rev. Lett.* **2006**, *97*, 170201.
- (47) Umari, P.; Pasquarello, A. Ab initio Molecular Dynamics in a Finite Homogeneous Electric Field. *Phys. Rev. Lett.* **2002**, *89*, 157602.
- (48) Perdew, J. P.; Wang, Y. Accurate and simple analytic representation of the electron-gas correlation energy. *Phys. Rev. B* **1992**, *45*, 13244–13249.